

## An adaptive wavelet-collocation method for shock computations

J. D. Regele & O. V. Vasilyev

To cite this article: J. D. Regele & O. V. Vasilyev (2009) An adaptive wavelet-collocation method for shock computations, International Journal of Computational Fluid Dynamics, 23:7, 503-518, DOI: [10.1080/10618560903117105](https://doi.org/10.1080/10618560903117105)

To link to this article: <https://doi.org/10.1080/10618560903117105>



Published online: 14 Sep 2009.



Submit your article to this journal [↗](#)



Article views: 399



Citing articles: 27 View citing articles [↗](#)

## An adaptive wavelet-collocation method for shock computations

J.D. Regele and O.V. Vasilyev\*

Department of Mechanical Engineering, 427 UCB, University of Colorado, Boulder, CO 80309-0427, USA

(Received 5 August 2008; final version received 7 June 2009)

A simple and robust method for solving hyperbolic conservation equations based on the adaptive wavelet-collocation method, which uses a dynamically adaptive grid, are presented. The method utilises natural ability of wavelet analysis to sense localised structures and is based on analysis of wavelet coefficients on the finest level of resolution to create a discontinuity locator function  $\Phi$ . Using this function, an artificial viscous term is explicitly added in the needed regions using a localised numerical viscosity that ensures the positivity and TVD non-linear stability conditions. Once the wavelet coefficients on the finest level of resolution are below the error threshold parameter  $\epsilon$ , the artificial viscosity is shut off and any remaining physical waves are free to propagate undamped. Multiple examples in one and two dimensions are presented to demonstrate the method's robustness, simplicity and ease of extending to more complex problems.

**Keywords:** Euler equations; hyperbolic conservation laws; wavelets; adaptive grid; artificial viscosity; Riemann problem; shock capturing

### 1. Introduction

Although computer technology continues to grow at a rapid rate, computer processor speeds continue to be a limiting factor in numerical modelling of science and engineering applications. Various approaches have been developed to remedy this problem, however they do not come without a cost. If a uniform grid is used, it is not unusual to find that expensive and complicated flux calculations are required to increase the efficiency. Traditionally with non-uniform or unstructured grids, a mesh generator is required or ad-hoc rules and assumptions are needed for adaptive mesh refinement (Babuska *et al.* 1984, Flaherty 1989).

The numerical solution of hyperbolic conservation laws presents an added level of difficulty because of their inherent nature to form jump discontinuities. The number of techniques and algorithms available to address these problems are abundant in the literature. However, there exists a major commonality among most of the more traditional schemes and that is the use of artificial viscosity. The simplest means of resolving a shock is by artificially increasing the physical viscosity in the discontinuity regions to avoid unphysical oscillations. This approach requires a very fine grid in order to obtain sharp discontinuity and is impractical unless a non-uniform grid is used (e.g. Woodward and Colella 1984, Nithiarasu and *et al.* 1998). Examples of the modern methods used

today include Harten, Lax and van Leer (HLLC) (Harten *et al.* 1983), essentially non-oscillatory (ENO) (Harten *et al.* 1997), weighted essentially non-oscillatory (WENO) (Liu *et al.* 1994) schemes, monotone upstream-centred schemes for conservation laws (MUSCL) (van Leer 1979, Colella 1985), advection upstream splitting method (AUSM) (Liou and Steffen 1993, Liou 1996). For more details of these and other schemes, we refer to Toro (1997), Laney (1998). It is well known from Godunov's theorem (Toro 1997) that it is impossible to have a monotonic linear method that is higher than first order accurate. All approaches mentioned earlier use information obtained from the solution to create non-linear schemes so that higher accuracy is achieved. Most high order schemes such as MUSCL use subgrid scale data reconstruction, which substantially increases the numerical cost.

Harten (1994) introduced the use of wavelets as a new compression algorithm to reduce the number of points needed to solve the compressible Euler equations. A standard central differencing flux was used for regions of low resolution. In the shock regions, the method was switched to a simplified ENO scheme. Harten demonstrated that the magnitude of a wavelet coefficient is of the same order as the jump discontinuity. Furthermore, the local Lipschitz exponent can be obtained from the wavelet coefficients to ascertain further information about the

---

\*Corresponding author. Email: oleg.vasilyev@colorado.edu

regularity of the solution (Sjogreen and Yee 2000). Therefore, wavelet coefficients act as a good indicator of a shock's location. In the last few years, there has been a significant effort to incorporate the use of wavelet compression for the solution of hyperbolic partial differential equations using either finite volume formulation (Cohen *et al.* 2001, Chiavassa *et al.* 2003) or WENO scheme (Burger and Kodakevicius 2007) combined with a multiresolution technique based on interpolating wavelets (Donoho 1992, Harten 1994). It is clear from these and other works on the use of adaptive meshes for shock computations (e.g. Warren *et al.* 1991, 1993, Yamaleev and Carpenter 2002) that fully adaptive multiresolution schemes offer a clear computational advantage over conventional schemes.

Over the last several years, our research group has developed an adaptive wavelet-collocation method (AWCM) (Vasilyev and Bowman 2000, Vasilyev 2003, Vasilyev and Kevlahan 2005) that is based on second generation wavelets (Sweldens 1996, 1998). The method has been successfully applied to the solution of both parabolic (Vasilyev and Kevlahan 2002, Alam *et al.* 2006, Kevlahan *et al.* 2007) and elliptic partial differential equations (Vasilyev and Kevlahan 2005). This article is the extension of the AWCM to hyperbolic differential equations. The overall philosophy of this work deviates from the current trend of computationally expensive high order schemes and takes advantage of the dramatic savings achieved with a dynamically adaptive multi-resolution grid to resolve discontinuities so that the wavelet coefficients in discontinuity regions remain in a specified range. This is achieved by taking the shock capturing approach, which explicitly adds artificial viscosity to smoothen shocks and applies it in a manner more reminiscent of a flux-limiting method (van Leer 1979). The main advantage of this approach is that the AWCM is used to reduce memory overhead and computational costs significantly to obtain a simple method that avoids any elaborate flux manipulations. The method may not be capable of resolving shocks and contacts in as few grid cells as some more elaborate schemes (e.g., Colella 1985, Liu *et al.* 1994, Liou 1996), but since the AWCM significantly reduces the number of grid points, the approximation of discontinuities on a wider stencil is justified. It should be noted that the proposed shock capturing scheme can be used in the context of Adaptive Mesh Refinement methods (Berger and Olinger 1984, Berger and Colella 1989, Bell *et al.* 1994, Berger and Leveque 1998) with wavelet-based shock locator function used for all highest resolution patches. However, the use of patches wider than the number of points required for stable shock capturing would reduce the computational efficiency of the proposed methodology. The

purpose of this work is to develop a general and robust algorithm to solve hyperbolic equations in conjunction with the AWCM while still maintaining its error thresholding properties.

This article is organised in the following manner. First in Section 2 a brief overview of the AWCM is given and its error thresholding properties are discussed. The hyperbolic solver, including the wavelet-based shock locator function, is described in Section 3. The results of a series of one- and two-dimensional tests are discussed in Section 4. Finally, a summary of the overall conclusions is given in Section 5.

## 2. Adaptive wavelet collocation method

The numerical technique introduced in this study directly uses the AWCM (Vasilyev and Bowman 2000, Vasilyev 2003), which utilises second generation wavelets to efficiently solve partial differential equations. Until now, compressible flow simulations using this method were limited to solving full Navier–Stokes equations. As the Reynolds number increases, so does the number of grid points required to resolve a shock. In this work, a hyperbolic solver is developed that is capable of solving Euler equations in a manner that still takes advantage of the method's strengths, yet its implementation is simple and robust.

It is well known (Daubechies 1992, Chui 1997, Mallat 1998) that any function  $u(\mathbf{x})$  in an  $n$ -dimensional space can be decomposed as

$$u(\mathbf{x}) = \sum_{\mathbf{k} \in \mathcal{K}^0} c_{\mathbf{k}}^0 \phi_{\mathbf{k}}^0(\mathbf{x}) + \sum_{j=0}^{+\infty} \sum_{\mu=1}^{2^n-1} \sum_{\mathbf{l} \in \mathcal{L}^{\mu,j}} d_{\mathbf{l}}^{\mu,j} \psi_{\mathbf{l}}^{\mu,j}(\mathbf{x}) \quad (1)$$

where  $c_{\mathbf{k}}^0$  and  $\phi_{\mathbf{k}}^0(\mathbf{x})$  are the scaling coefficients and functions on the lowest level of resolution and  $d_{\mathbf{l}}^{\mu,j}$ ,  $\psi_{\mathbf{l}}^{\mu,j}(\mathbf{x})$  are the wavelet coefficients and basis functions, bold roman subscripts denote index in  $n$ -dimensional space, *i.e.*  $\mathbf{k} = (k_1, \dots, k_n)$ ,  $\mathcal{K}^0$  and  $\mathcal{L}^{\mu,j}$  are  $n$ -dimensional index sets associated with scaling functions at zero level of resolution and wavelets of family  $\mu$  and level  $j$ . Because of the fact that most of the shock type problems involve very localised jump discontinuities with smooth solutions elsewhere, wavelet-type numerical methods are a great candidate for solving these problems. Most wavelet coefficients  $d_{\mathbf{l}}^{\mu,j}$  will be small except near jump discontinuities. Equation (1) can be decomposed into two terms whose wavelet coefficients are above and below a threshold parameter  $\epsilon$ ,

$$u(\mathbf{x}) = u_{\geq}(\mathbf{x}) + u_{<}(\mathbf{x}), \quad (2)$$

where

$$u_{\geq}(\mathbf{x}) = \sum_{\mathbf{k} \in \mathcal{K}^0} c_{\mathbf{k}}^0 \phi_{\mathbf{k}}^0(\mathbf{x}) + \sum_{j=0}^{+\infty} \sum_{\mu=1}^{2^n-1} \sum_{\substack{\mathbf{l} \in \mathcal{L}^{\mu,j} \\ |d_1^{\mu,j}| \geq \epsilon \|u\|}} d_1^{\mu,j} \psi_1^{\mu,j}(\mathbf{x}), \quad (3)$$

$$u_{<}(\mathbf{x}) = \sum_{j=0}^{+\infty} \sum_{\mu=1}^{2^n-1} \sum_{\substack{\mathbf{l} \in \mathcal{L}^{\mu,j} \\ |d_1^{\mu,j}| < \epsilon \|u\|}} d_1^{\mu,j} \psi_1^{\mu,j}(\mathbf{x}). \quad (4)$$

Donoho (1992) was able to show that for a regular function the error is bounded as

$$\|u(\mathbf{x}) - u_{\geq}(\mathbf{x})\| \leq C_1 \epsilon \|u\|, \quad (5)$$

which means that the number of grid points needed to solve a numerical problem can be significantly reduced while still retaining a prescribed level of accuracy determined by the threshold parameter  $\epsilon$ .

Estimation (5) is based upon the assumption that the solution is a regular function. Hyperbolic conservation laws naturally produce discontinuous solutions, which require infinitely fine mesh to properly represent them numerically. Limiting the maximum level of resolution results in undesirable oscillatory Gibbs phenomena in the vicinity of a discontinuity (e.g. Vasilyev *et al.* 1995). One way to prevent these oscillation is to add numerical diffusion in the immediate proximity to the shock. It should be noted that by setting a maximum level of resolution and adding artificial viscosity in the discontinuity region effectively create an upper bound on the wavelet coefficients  $d_1^{\mu,j}$ . Because the wavelet coefficients determine how rapidly a function can change, limiting the coefficients improve an upper bound on a shock steepness. When this artificial viscosity is applied in a systematic manner, approximately the same number of points are needed in order to resolve a shock. Each time the level of resolution is increased, the width of the shock decreases by a factor of 2. If  $j_{\max}$  is set reasonably high, the scales resolved by the algorithm will approach the physical scales but will still be under-resolved for the sake of numerical stability.

### 3. Hyperbolic solver

The objective of this article is to develop a dynamically adaptive hyperbolic solver in conjunction with the AWCM that is robust and simple to implement.

Because of the computational advantage that wavelets provide, artificial viscosity is explicitly added near shocks and discontinuities to smoothen them over several points. Many foundational techniques use flux or wave speed splitting to ensure that the upwind techniques are applied in the correct characteristic directions. These upwind techniques introduce an implicit artificial viscosity term that provides the non-linear numerical stability condition needed when solving hyperbolic conservation laws. The current research effort seeks to avoid using these techniques as they become difficult to use when dealing with a dynamically adaptive grid. The proposed method, which is similar to Harten's switching criteria (Harten 1994), determines a shock's location by its wavelet coefficient on the finest level of resolution. Using the coefficients, a shock locator type function  $\Phi$  is created to explicitly add artificial viscosity in the vicinity of a discontinuity or shock. The combination of these different ideas with the dynamically adaptive grid creates a computational scheme that is highly versatile, yet accurate to a predetermined level. The time integrations are performed using an implicit Krylov technique and the time step  $\Delta t$  is still calculated using the CFL condition based upon the smallest grid spacing  $\Delta x$  on the finest scale. However, the CFL restriction does not come from the classical stability analysis, as the integration scheme is implicit and is capable of using larger time-steps. The CFL limitation comes from adaptive nature of the algorithm, namely time step is restricted by the requirement that small-scale structures do not move outside of high resolution regions within a time step, thus insuring the proper resolution of flow structures during time integration. Further details about time integration with the dynamically adaptive grid can be found in previous work (Vasilyev and Bowman 2000, Vasilyev 2003, Kevlahan and Vasilyev 2005).

#### 3.1. Shock locator function

Harten (1994) demonstrated that the magnitude of a wavelet coefficient is proportional to the size of a jump discontinuity making wavelet coefficients a good indicator of a shock's location. Flux limiting methods (e.g. van Leer 1974, Sweby 1984, Yee 1987) have all varied their flux-limiting functions with their neighbouring points using either conserved variables or flux differences. Using these limiters they would limit the artificial viscosity applied in smooth regions and allow large amounts near jump discontinuities.

In general, the one dimensional flux-limiting conservation equations can be written as

$$\frac{\partial \mathbf{u}}{\partial t} + \frac{\partial \mathbf{f}}{\partial x} = \frac{\partial}{\partial x} \left( v(\Phi) \frac{\partial \mathbf{u}}{\partial x} \right), \quad (6)$$

where the viscosity  $\nu$  is a function of the flux limiter  $\Phi$ . In this work, the flux limiter, also called the shock locator function  $\Phi$ , varies with the magnitude of the wavelet coefficients. Instead of changing the method of calculating our flux in the shock region, we gradually introduce viscosity explicitly in order to smoothen the shock over several points and reduce any spurious oscillations to values below our error threshold parameter  $\epsilon$ . Recall from Section 2 that because  $\mathbf{u}$  is decomposed into wavelet coefficients and their basis functions, the entire solution is oscillatory in nature. However, the magnitude of these oscillations is governed by a prescribed error threshold parameter. It is imperative that the oscillations introduced by a jump discontinuity are damped below  $\epsilon$ , otherwise the oscillations will remain in the solution indefinitely. The limiter function  $\Phi$  is calculated using two parameters, the wavelet coefficient threshold parameter  $\epsilon$  and a diffusive threshold parameter  $\epsilon_d$ . Using this parameter we calculate a vector of shock locators  $\Phi$  for each variable according to the equation

$$\Phi_k = \begin{cases} \frac{|\mathbf{d}_k^{j_{\max}}|}{\|\mathbf{u}\|} & \text{for } 0 < |\mathbf{d}_k^{j_{\max}}| \leq \epsilon_d \|\mathbf{u}\|, \\ 1 & \text{for } |\mathbf{d}_k^{j_{\max}}| > \epsilon_d \|\mathbf{u}\| \end{cases}, \quad (7)$$

It was found that having one global shock locator taken as a maximum value for each of the variables defined by

$$\Phi_k = \max(\Phi_k) \quad (8)$$

produces as good results with substantial reduction of memory. Here,  $\Phi_k$  represents the vector of shock locator functions for each conserved variable in  $\mathbf{u}$ . The final scalar locator function  $\Phi_k$  is chosen as the maximum over different variables. Each component is scaled by a normalisation factor  $\|\mathbf{u}\|$ . In order to stay within the computational memory limits, a particular computer may possess, it is necessary to set a maximum level of resolution  $j_{\max}$ . Until the finest level of resolution is reached, a standard central differencing flux is used to prevent any dissipation away from jump discontinuities.

To impose an upper bound on the wavelet coefficients in the discontinuity regions, a user defined parameter,  $\epsilon_d$ , is introduced (see Equation (7)). As this value is reduced the discontinuities become more smooth. If it is increased, the viscosity is reduced and steeper more oscillatory discontinuities are observed. For the current work, the parameter  $\epsilon_d$  is needed to ensure the minor oscillations that are present in the solution are bounded. A general rule of thumb for prescribing this parameter is  $\epsilon_d = 10\epsilon$ , where again  $\epsilon$  is the overall error threshold parameter.

As was previously noted the AWCM is based on second generation wavelets (Sweldens 1996, 1998),

which results in one-to-one correspondence between grid points and wavelet coefficients. Because hyperbolic conservation laws would require infinite levels of resolution to obtain an exact solution, our refinement is limited to a finite level  $j_{\max}$ . Until this level is reached the solution's error is bounded by the error threshold parameter  $\epsilon$ . If the solution starts using points at the finest level of resolution and the corresponding wavelet coefficients are larger than the threshold parameter, spurious oscillations could occur. It is for this reason that the wavelet coefficients at the  $j_{\max}$  level are used to determine where artificial viscosity should be applied.

The neighbouring points at levels  $j < j_{\max}$  as described in (Vasilyev and Paolucci 1996, 1997) cannot provide the information needed to distinguish whether there is a discontinuity present or not. As a result, calculation of  $\Phi_k$  for all levels  $j < j_{\max}$  is performed by assigning it the value of the maximum wavelet coefficient of its surrounding neighbours at the  $j_{\max}$  level. Because of dyadic nature of wavelet decomposition, the wavelet coefficients only present at every other point on the computational mesh. To bypass this problem, a positivity preserving low-pass filter is applied to smoothen the shock locator function. Figure 1 shows a typical shock and its corresponding  $\Phi$ . Notice that the shock locator is located only at the shock and not the contact line or corners of the expansion wave. This is due to the fact that the wavelet coefficients associated with those regions are small enough so that viscosity is not needed in those regions in order to maintain the prescribed level of accuracy. It should be noted that artificial viscosity is added at those locations during the initial stages of the solution until the error is reduced below the threshold. For consistency, it should be understood that the locator function  $\Phi$ , used in the rest of this article, is actually a spatially averaged function.

### 3.2. Numerical technique

Because of the intentional simplicity of this scheme, let us start by considering the scalar conservation equation

$$\frac{\partial u}{\partial t} + \frac{\partial f}{\partial x} = 0. \quad (9)$$

Upon discretising the flux at the  $x_i$  location using second-order central differencing and adding diffusive terms from Equation (6), written in conservative form, Equation (9) becomes

$$\frac{\partial u_i}{\partial t} = -\frac{f_{i+1} - f_{i-1}}{2\Delta x} + \frac{v_{i+1/2} \frac{u_{i+1} - u_i}{\Delta x} - v_{i-1/2} \frac{u_i - u_{i-1}}{\Delta x}}{\Delta x}. \quad (10)$$



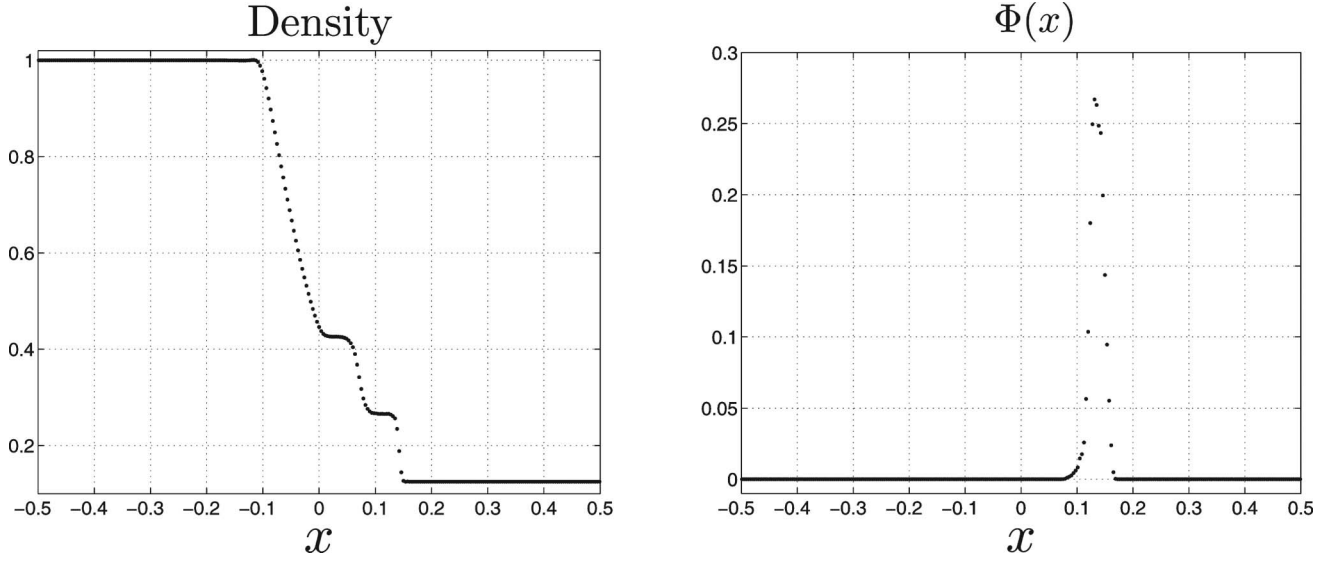


Figure 1. A typical  $\Phi$  function is shown on the right coincident with the shock front shown on the left.

The equation can be rewritten in standard explicit form with the minimum amount of viscosity required by the non-linear stability condition (Laney 1998)

$$\frac{\partial u_i}{\partial t} = -\frac{f_{i+1} - f_{i-1}}{2\Delta x} + \frac{1}{2} \left( |a_{i+1/2}| \frac{u_{i+1} - u_i}{\Delta x} - |a_{i-1/2}| \frac{u_i - u_{i-1}}{\Delta x} \right), \quad (11)$$

where the advection velocity is defined as

$$a_{i+1/2} = \begin{cases} \frac{f(u_{i+1}) - f(u_i)}{u_{i+1} - u_i} & u_{i+1} \neq u_i \\ f'(u_i) & u_{i+1} = u_i \end{cases}. \quad (12)$$

Equation (11) is easily implemented using the scalar conservation law, but when solving Euler equations, the artificial viscosity application becomes non-trivial. In the case of Euler equations, the scalar  $a_{i+1/2}$  is typically replaced with the Jacobian matrix  $\mathbf{A}_{i+1/2}$ . Historically, it is common to use some approximation such as the Roe-averaged Jacobian or some secant plane slope matrix (Laney 1998). In order to keep the algorithm simple, the one-wave technique is employed, which replaces  $a_{i+1/2}$  with the maximum characteristic  $|u_{i+1/2}| + c_{i+1/2}$  denoted as  $A_{i+1/2}$ . Although this technique ensures adequate stability for shocks, it damps contact discontinuities more than needed. However, due to not self-sustaining nature of contact discontinuity, the numerical viscosity is automatically reduced to zero after few time steps. By making

this change, Equation (11) can be written in a vector form as

$$\frac{\partial \mathbf{U}_i}{\partial t} = -\frac{\mathbf{F}_{i+1} - \mathbf{F}_{i-1}}{2\Delta x} + \frac{1}{2} A_{i+1/2} \frac{\mathbf{U}_{i+1} - \mathbf{U}_i}{\Delta x} - \frac{1}{2} A_{i-1/2} \frac{\mathbf{U}_i - \mathbf{U}_{i-1}}{\Delta x} \quad (13)$$

with the scalar velocity coefficient defined as

$$A_i = |u_i| + c_i, \quad (14)$$

where  $c_i$  is the speed of sound at the  $x_i$  location and the mid-point values are calculated using

$$A_{i+1/2} = \max(A_i, A_{i+1}). \quad (15)$$

The conserved variables at the  $i^{\text{th}}$  location are written as  $\mathbf{U}_i$  so that they are not confused with the velocity  $u$  and the flux vectors are written as  $\mathbf{F}$ . If Equation (13) is written in a wave speed split form it is relatively simple to verify that the scheme satisfies Harten's positivity condition (Harten 1983). It is important to ensure that the artificial viscosity is strong enough to reduce oscillations as time progresses. Because the positivity condition is stronger than the TVD condition it is safe to say that the scheme should provide enough artificial viscosity to reduce any oscillations below the threshold  $\epsilon$ . It is important to note that there indeed will be oscillations in the solution of the order of  $\epsilon$  because of interpolation error introduced by wavelet thresholding, however the artificial viscosity is used whenever

necessary to maintain those oscillations at a prescribed magnitude.

The flux in relation (13) still assumes the form of a simple second order accurate central differencing scheme. Flux limiting methods normally switch between two different fluxes, one of high order and one of low order, which can preserve monotonicity. As the artificial viscosity is written as an explicit addition, the algorithm will only maintain its monotonicity properties as long as the flux remains second order accurate. In general, fluxes of higher than second order accuracy will be employed, e.g. fourth or sixth order. This is where the scheme deviates from a flux-limiting method and appears more like a shock capturing viscosity scheme. Once the flux becomes of arbitrary order, it no longer maintains its monotonicity preserving properties. In order to aid in reducing the oscillations, the scheme may have an upper bound  $\epsilon_d$  introduced in Equation (7) to make sure that the magnitude of the wavelet coefficients never rise above that value. Setting this value is a bit artificial but it serves the purpose of ensuring a smooth transition across self-sustaining discontinuities. A general rule of thumb is to use  $\epsilon_d$  approximately an order of magnitude larger than the general error threshold parameter  $\epsilon$ .

Remember that the viscosity is only applied in the jump discontinuity regions. The flux limiter  $\Phi$  is combined along with the general flux limiting method described in (Laney 1998) to obtain

$$\frac{\partial \mathbf{U}_i}{\partial t} = - \frac{\partial \mathbf{F}_i}{\partial x} + \frac{v_{i+1/2} \frac{\mathbf{U}_{i+1} - \mathbf{U}_i}{\Delta x} - v_{i-1/2} \frac{\mathbf{U}_i - \mathbf{U}_{i-1}}{\Delta x}}{\Delta x}, \quad (16)$$

$$v_{i+1/2} = \frac{1}{2} \Phi_{i+1/2} (c_{i+1/2} + |u_{i+1/2}|) \Delta x, \quad (17)$$

where the flux term  $\frac{\partial \mathbf{F}_i}{\partial x}$  is a standard central differencing operator of arbitrary accuracy. In practice, a fourth order central differencing operator is generally used. Wavelet decomposition is used for grid adaptation and interpolation, whereas a hierarchical finite difference scheme, which takes advantage of wavelet multilevel decomposition, is used for derivative calculations (Vasilyev and Bowman 2000). Note that in order to further improve the performance of the shock capturing scheme the minimum value of  $c_{i+1/2} + |u_{i+1/2}|$  was bounded by the maximum value of  $\Phi_{i+1/2} c_{i+1/2}$ , denoted by  $\|c\Phi\|_\infty$ . Thus, the final form of the numerical viscosity is given by

$$v_{i\pm 1/2} = \frac{1}{2} \Phi_{i\pm 1/2} \max \{ (c_{i\pm 1/2} + |u_{i\pm 1/2}|), \|c\Phi\|_\infty \} \Delta x. \quad (18)$$

### 3.2.1. Multiple dimensions

In multiple dimensions, the shock capturing scheme is applied in tensorial manner, i.e. the final scheme given in Equations (16) and (18) is generalised into the form of Equation (6) with the diffusive terms for the  $n$ -dimensional case symbolically written as

$$\sum_{k=1}^n \frac{\partial}{\partial x_k} \left( v_k \frac{\partial \mathbf{U}}{\partial x_k} \right), \quad (19)$$

$$v_k = \frac{1}{2} \Delta x_k \Phi C, \quad (20)$$

$$C = \max \{ (c + \sqrt{u_k u_k}), \|c\Phi\|_\infty \}, \quad (21)$$

where derivatives are assumed to be applied in different directions as in relation (16). Note that for notational convenience, we use roman subscript to denote grid point index and italic subscript to denote the direction or vector component. Also note that there are  $n$  different  $v_k$  values, where each is proportional to its respective direction's grid spacing. In addition, the characteristic velocity is a scalar quantity. Although it is possible to use characteristic velocities in each respective direction, this often results in solution decoupling between directions and increases the number of grid points.

## 4. Numerical results

In order to demonstrate the strengths of this technique, results are presented in two different sections. The first section will present only 1-dimensional examples of standard Riemann problems where an exact solution is available for comparison. This section demonstrates the power of the AWCN in conjunction with this technique and shows that the error is truly bounded by the threshold parameter  $\epsilon$ . The second section presents a numerical simulation of the 2-dimensional Richtmyer–Meshkov instability that demonstrates how easily the method is implemented in multiple dimensions as well as extended to more difficult problems. Note that in all one-dimensional plots the numerical solution is interpolated to uniform grid for better comparison with the analytical solution. In actual simulations only a small fraction of grid points is used.

### 4.1. One-Dimensional Riemann problems

Each of the following examples is solved on computational meshes with effective resolution of 320, 640 and 1280 points corresponding to  $j_{\max}$  levels of 4, 5 and 6,

respectively. The diffusive threshold parameter  $\epsilon_d$  was set to be 0.01 and the CFL number is 1.0.

#### 4.1.1. Weak shock

The first test case is a simple weak shock tube problem as found in (Toro 1997) with the following initial conditions

$$\begin{aligned} \rho_L &= 1.0, & \rho_R &= 0.125, \\ u_L &= 0.0, & u_R &= 0.0, \\ p_L &= 1.0, & p_R &= 0.1. \end{aligned} \quad (22)$$

Figures 2–4 show the density at the final time of 0.24. Note that for each increase in the level of resolution  $j_{\max}$ , the thickness of the jump discontinuity decreases by a factor of 2. This is an expected result because the fact that the numerical solution is smooth and the artificial viscosity is proportional to  $\Delta x$ , which makes the method first order accurate at the finest level of resolution. It should also be noted that the simulation with  $j_{\max}$  of 4 uses 147 points while using an effective grid of 320 points. Increasing the level of resolution to  $j_{\max} = 5$ , giving an effective grid of 640 points only requires the use of 31 more points and one more

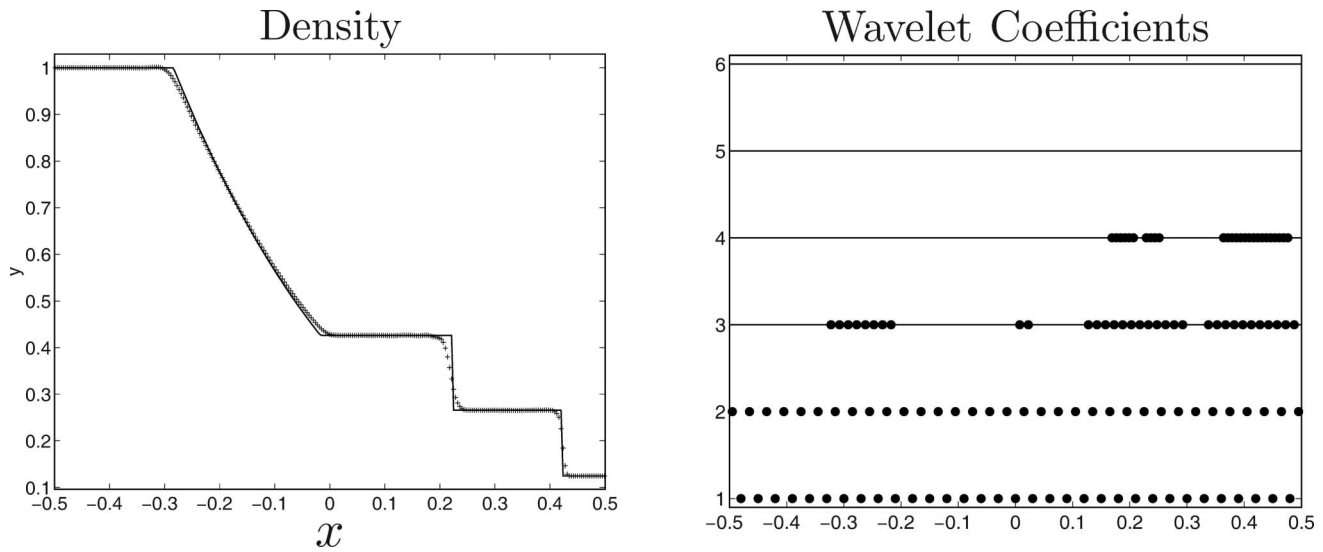


Figure 2. Left: density for weak shock problem at time 0.24;  $j_{\max} = 4$ . Solid line denotes analytical solution. Right: effective grid size is 320 points, 147 points (●) are used at output time.

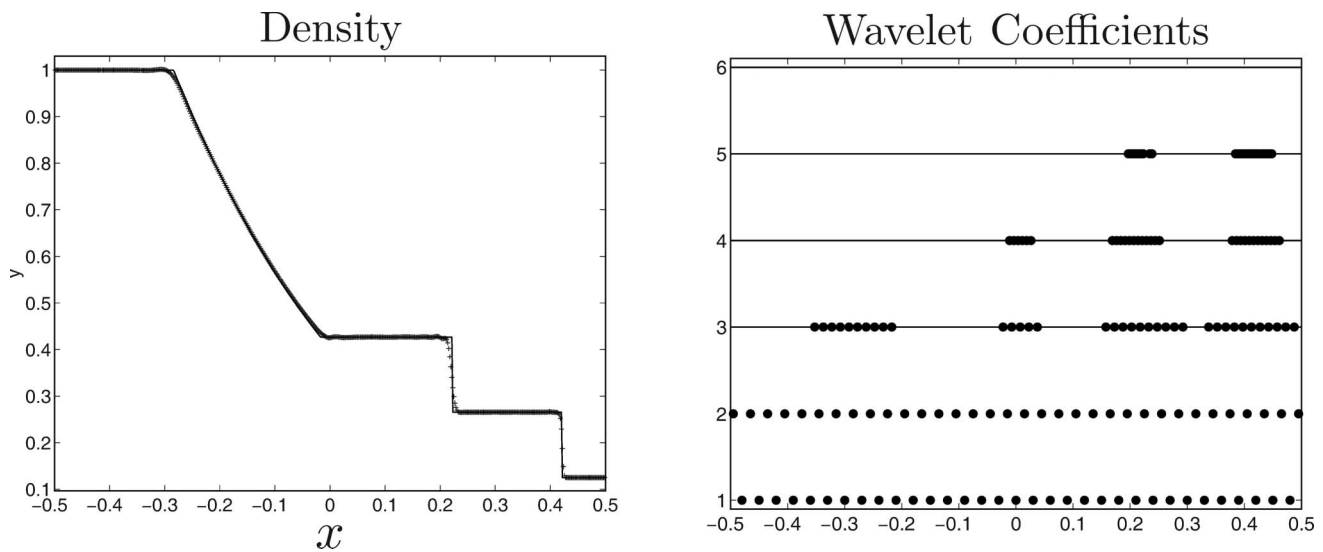


Figure 3. Left: density for weak shock problem at time 0.24;  $j_{\max} = 5$ . Solid line denotes analytical solution. Right: effective grid size is 640 points, 178 points (●) are used at output time.



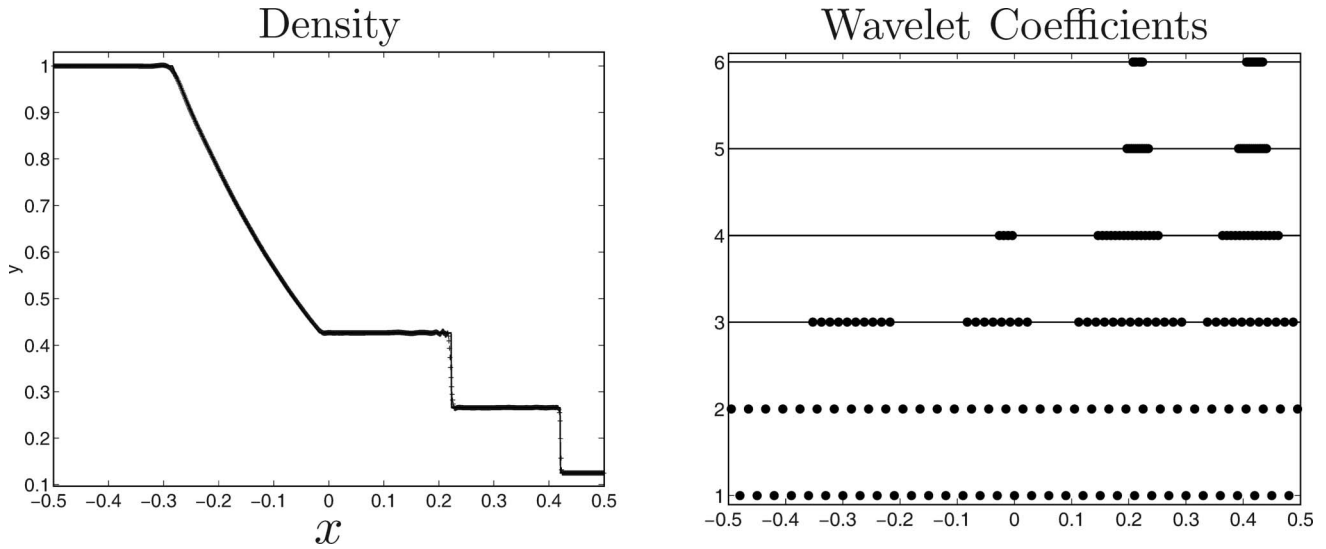


Figure 4. Left: density for weak shock problem at time 0.24;  $j_{\max} = 6$ . Solid line denotes analytical solution. Right: effective grid size is 1280 points, 208 points (●) are used at output time.

increase results in a grid of 1280 points using only 30 additional points. Remember that the density plots show the interpolated uniform grid solution, not the points used in the calculations. The wavelet coefficients that were used and saved are shown in the right plots.

In order to illustrate the local character of the error of the solution, the error between the numerical and the exact solutions is plotted in Figure 5 for simulations at four different resolutions. The thicknesses of the contact and shock decrease by a factor of 2 with each increase in the level of resolution. Notice that the corners of the expansion have a considerable error, especially in the low resolution cases. This is due to numerical diffusion experienced in the initial stages of the simulation, which are unavoidable because a first order shock capturing scheme is used. During the first few time steps, artificial viscosity is added at the initial jump discontinuity. At this point in time, the expansion, contact and shock waves are located in the artificial viscosity region, hence the damping that occurs affects both the contact and the expansion. Once enough time has passed the expansion and contact no longer need any artificial viscosity and remain undamped for the rest of the solution. It is important to note that once they reach the point where damping is no longer needed, they maintain their steepness for the entire duration of the simulation because there is now zero losses on those characteristics. When developing this technique, it was important to avoid unnecessary damping so that

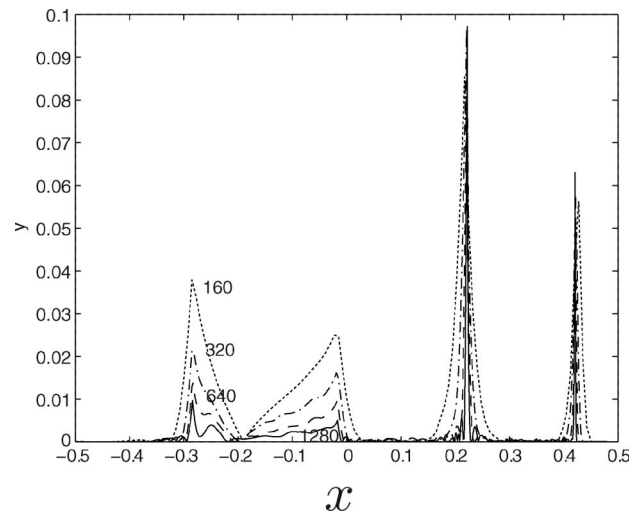


Figure 5. Local error of density for the weak shock for multiple levels of resolution. Effective grid sizes are 160, 320, 640 and 1280.

any acoustics or other phenomena may be able to exist without being damped away.

In previous work (Vasilyev and Bowman 2000, Vasilyev 2003), numerical tests were performed to verify the validity of the error threshold Equation (5) between simulations of uniform and non-uniform grids. It was shown that the overall simulation error decreased linearly with decreasing  $\epsilon$ . A similar set of tests were performed in this work to demonstrate that the error between the adaptive solution and the uniform solution are bounded by

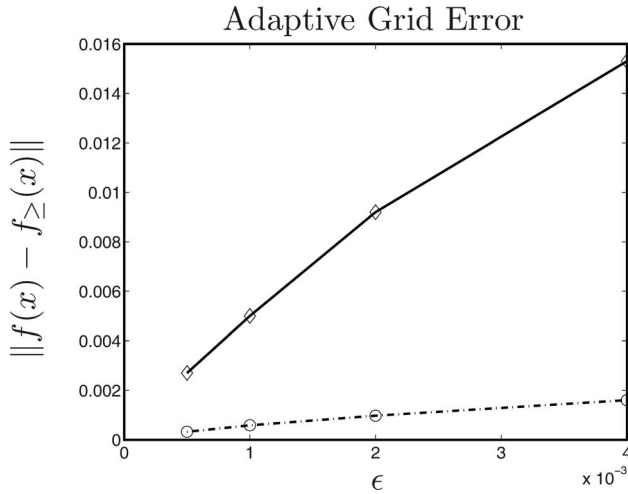


Figure 6.  $\mathcal{L}_\infty$  (—) and  $\mathcal{L}_2$  (---) differences between a uniform grid solution (320 points) and adaptive grid solutions with various threshold values. This shows a linear convergence with respect to  $\epsilon$ , which is consistent with previous adaptive algorithms.

relation (5). These tests were conducted by finding solutions for the weak shock tube problem using the new method on a uniform grid of 320 points. The diffusive threshold  $\epsilon_d$  is still 0.01 as with the adaptive grid solutions so that the schemes are consistent. Figure 6 shows the  $\mathcal{L}_\infty$  and the  $\mathcal{L}_2$  differences between the uniform and non-uniform grid solutions for the range of threshold values. It is readily seen that both norms decrease linearly with  $\epsilon$ . As a result, the technique still maintains its adaptive grid wavelet thresholding properties consistent with Equation (5).

Note that for all of the figures so far, the flux calculations are all of the 6th order. The steepness of the shocks and contacts are directly impacted by the order of the flux calculations. If the flux were only 2<sup>nd</sup> order, Equation (16) would be a standard first order upwind method. However, if a higher order flux is used there is a slight but noticeable improvement compared with the original upwind method as seen in Figure 7. Beyond the 4th order flux, the improvements are very slight and mostly noticeable in the spurious oscillations on the finest level of resolution. Although 8th or higher order accurate fluxes lead to further improvements of the amplitude of the spurious oscillations, its increased computational cost is not fully justified, as similar improvements can be obtained in a much more cost effective manner by using lower order flux with smaller error threshold parameter  $\epsilon$ . Thus, for practical purposes flux calculations should be limited to the 4th or 6th order.

#### 4.1.2. Strong shock

One of the main strengths of the AWC is its inherent ability to deal with multiple scales. The weak shock tube problem demonstrated all of the basic features it should have, but did not illustrate its ability to handle and stabilise stiff problems. In this section, the numerical method is applied to a strong shock tube problem found in (Toro 1997), where the initial conditions are

$$\begin{aligned} \rho_L &= 1.0, & \rho_R &= 0.01, \\ u_L &= 0.0, & u_R &= 0.0, \\ p_L &= 10.0, & p_R &= 0.01. \end{aligned} \quad (23)$$

Because of the increase in the strength and speed of the shock, the artificial viscosity applied at the shock location is much greater than before. Instead of all the scales being around 1, they vary from 0.01 up to 10.0. The effect of this change is that it makes the front of the shock appear to be moving faster than it should as shown in Figures 8 and 9. Note that the shock is not in fact moving faster than it should, it merely appears a few points ahead of the exact solution. This lead does not change as the solution progresses, it is simply a by-product of the large amount of artificial viscosity being applied in that region because of the large normalisation factors in relation (7). As the level of resolution increases, the error decreases by a factor of 2 until it is barely noticeable in Figure 10.

Figures 8–10 also show that the number of points needed to span the shock remains consistent with the number of points used in the weak shock problem, about 3–4 points. In this case the contact is much more damped than before due to the large amount of viscosity used on the shock. However, the method is adaptive and as the level of resolution is increased, the contact discontinuity returns to a shape closer to discontinuity with only few additional points added to the grid. Figure 8 uses 168 points but has an effective resolution of 320 points. Increasing the level of resolution once adds only 41 points but increases the effective grid to 640 points. Increasing the resolution further adds 30 more points and attains an effective grid of 1280 points.

#### 4.2. Two dimensional example

The equations for the evolution of two dimensional flows are written in terms of the conserved quantities  $\rho$ ,  $\rho u$ ,  $\rho v$  and the total energy  $\rho e_T$ . Writing them in vector form gives

$$\frac{\partial \mathbf{U}}{\partial t} + \frac{\partial \mathbf{F}(\mathbf{U})}{\partial x} + \frac{\partial \mathbf{G}(\mathbf{U})}{\partial y} = 0 \quad (24)$$

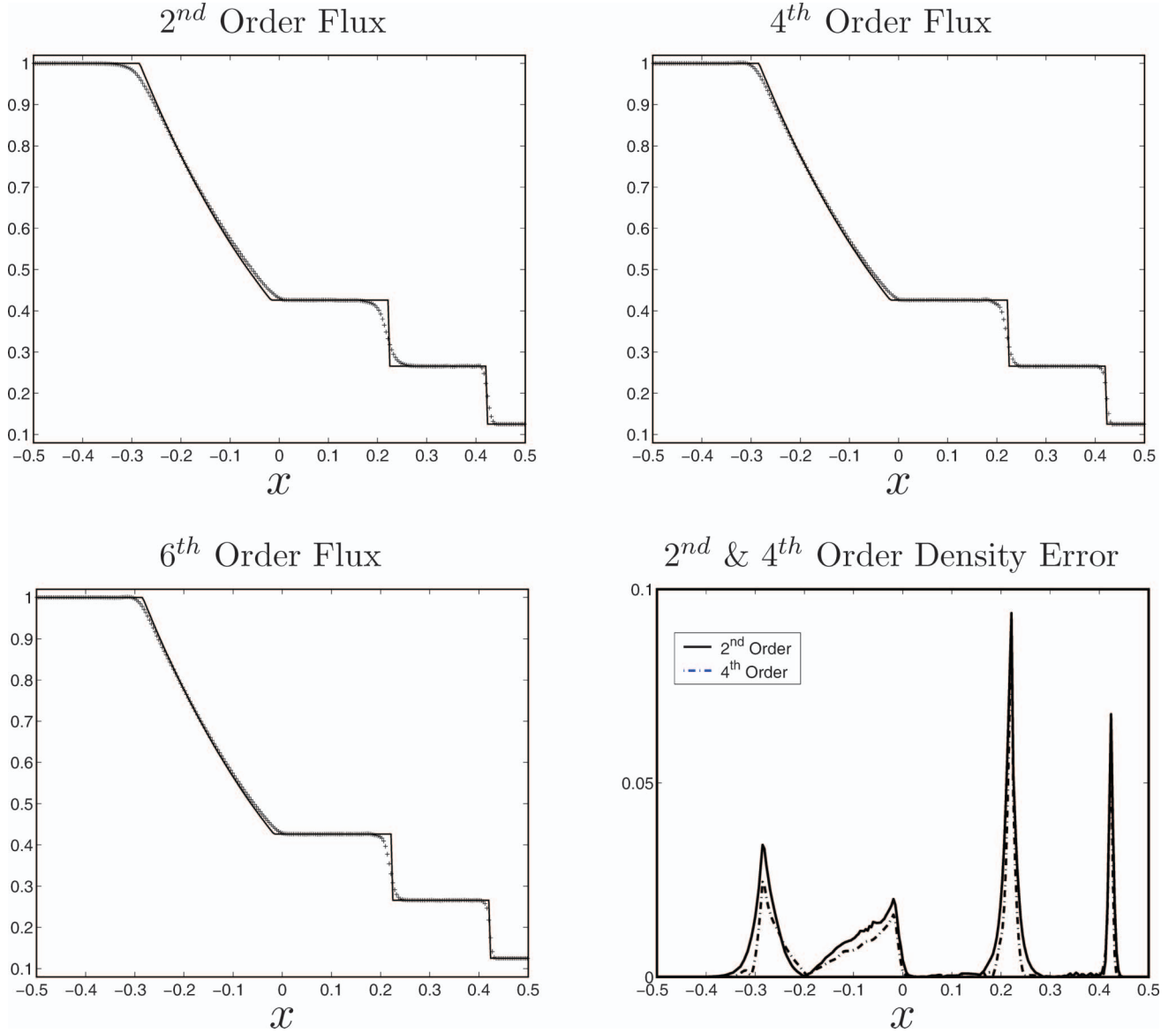


Figure 7. Density plots compared with exact solution on an effective grid of 320 points are shown for 2nd, 4th and 6th order flux calculations. The improvements beyond 4th order are mainly visible as spurious oscillation reductions. Solid line denotes analytical solution.

where  $\mathbf{U}$ ,  $\mathbf{F}(\mathbf{U})$  and  $\mathbf{G}(\mathbf{U})$  are defined as

$$\mathbf{U} = \begin{bmatrix} \rho \\ \rho u \\ \rho v \\ \rho e_T \end{bmatrix}, \quad \mathbf{F} = \begin{bmatrix} \rho u \\ \rho u^2 + P \\ \rho uv \\ (\rho e_T + P)u \end{bmatrix}, \quad (25)$$

$$\mathbf{G} = \begin{bmatrix} \rho v \\ \rho vu \\ \rho v^2 + P \\ (\rho e_T + P)v \end{bmatrix}$$

and the pressure is given by

$$P = (\gamma - 1) \left( \rho e_T - \frac{1}{2} \rho (u^2 + v^2) \right), \quad (26)$$

where  $\gamma$  is the ratio of specific heats.

The general vector formulation shown in Equation (24) can be rewritten by adding the conservative artificial viscosity terms resulting in

$$\begin{aligned} \frac{\partial \mathbf{U}}{\partial t} + \frac{\partial \mathbf{F}(\mathbf{U})}{\partial x} + \frac{\partial \mathbf{G}(\mathbf{U})}{\partial y} \\ = \frac{1}{2} \sum_{k=1}^n \Delta x_k \frac{\partial}{\partial x_k} \left( \Phi C \frac{\partial \mathbf{U}}{\partial x_k} \right) \end{aligned} \quad (27)$$

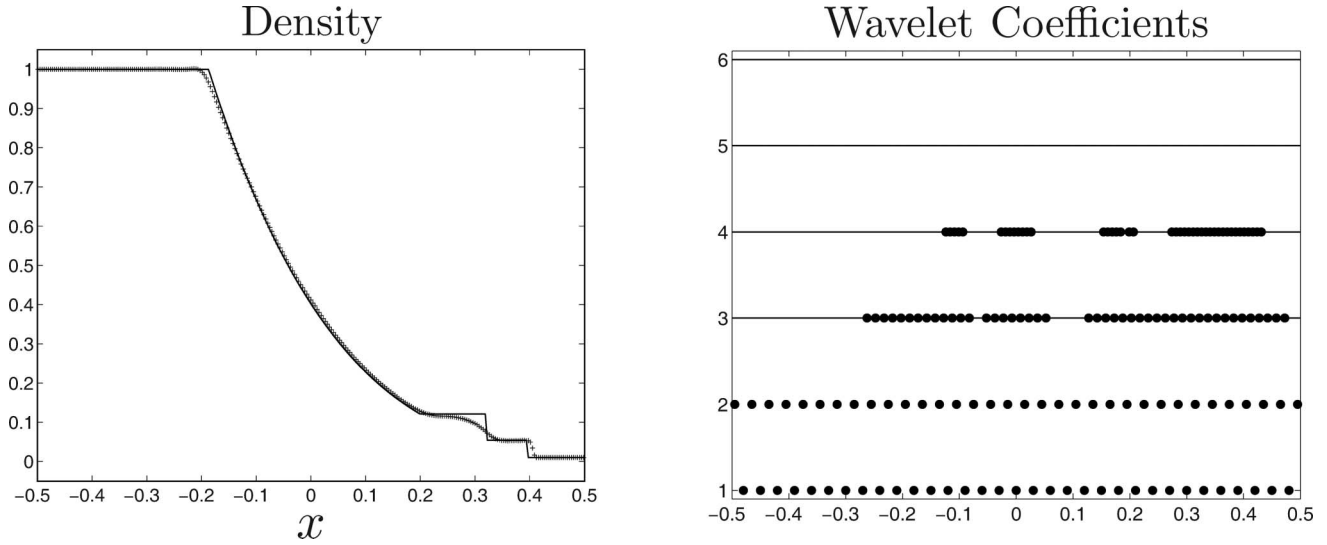


Figure 8. Density for strong shock problem at time 0.05;  $j_{\max} = 4$ , effective grid size is 320 points, 168 points (●) are used at output time.

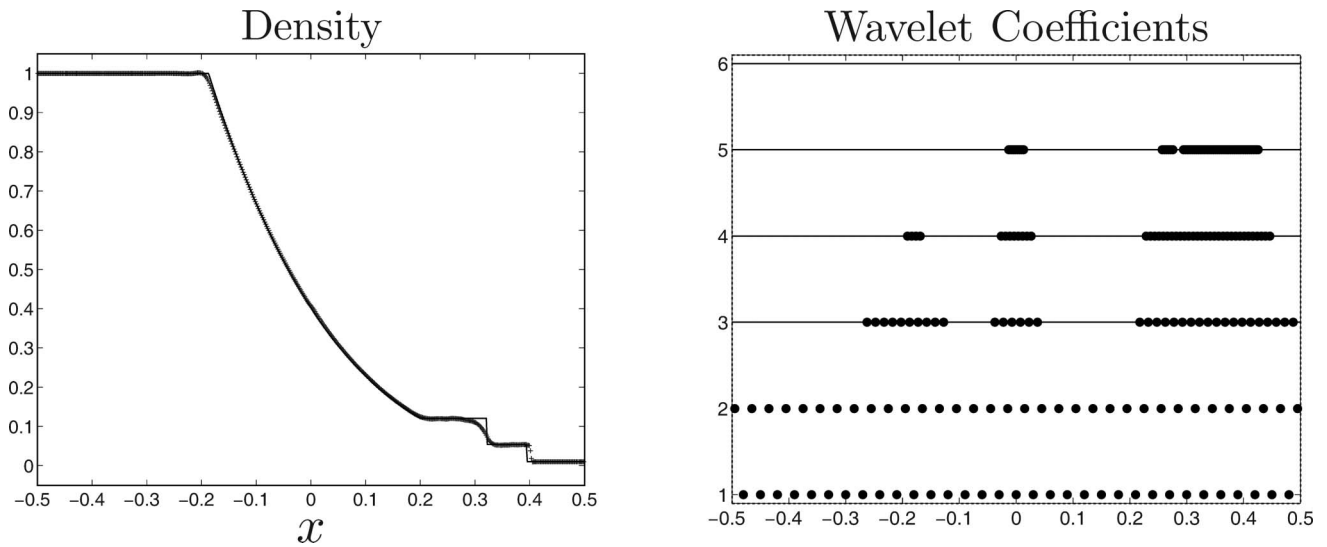


Figure 9. Density for strong shock problem at time 0.05;  $j_{\max} = 5$ , effective grid size is 640 points, 209 points (●) are used at output time.

where  $C$  is the maximum scalar characteristic given by Equation (21) with a sound speed  $(\gamma P/\rho)^{1/2}$ .

#### 4.2.1. Richtmyer–Meshkov instability

The ability of the proposed shock capturing approach to solve complex flows involving multi-component gas mixtures is illustrated by solving two-dimensional Richtmyer–Meshkov instability problem at Atwood number of 0.67, which was shown by Abarzhi and Herrmann (2003) to produce a mushroom vortex shape commonly associated with instability. The impinging shock has a Mach number of  $M = 1.5$  and

the interface is sinusoidal, similar to that seen in (Anuchina *et al.* 2004). For added complexity, different specific heat ratios were used for each fluid. In the starting fluid  $\gamma_1 = 1.4$  and in the second fluid  $\gamma_2 = 1.67$ . The computational domain is  $[0, 4] \times [-1, 1]$ . Figure 11 shows the initial condition. Note that the problem is solved in a moving reference frame so that the instability forms in the centre of the computational domain. The pressure, density and velocity are prescribed in region I and all other quantities can be calculated using standard shock relations and the fact that the material interface is at thermal equilibrium. A mass fraction ( $Y_i$ ) formulation is used and  $Y_1 = 1$ ,

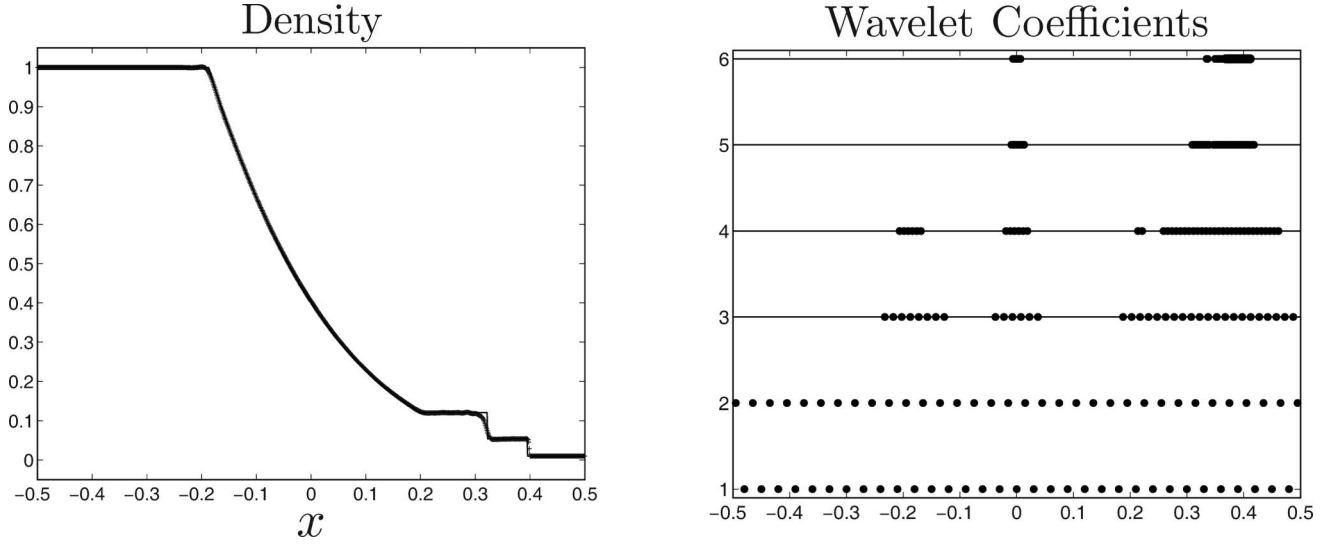


Figure 10. Density for strong shock problem at time 0.05;  $j_{\max} = 6$ , effective grid size is 1280 points, 239 points (●) are used at output time.

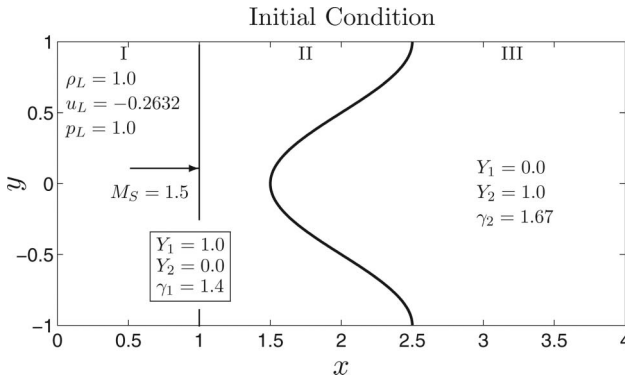


Figure 11. Initial condition of Richtmyer–Meshkov instability. Region I is the incoming flow producing the  $M = 1.5$  shock wave. Region II is the gas between the impinging shock and the material interface with region III. Atwood number for the interface is  $At = 0.67$ .

$Y_2 = 0$  in regions I and II and vice versa for region III. The interface location between regions II and III is given by  $x_{int} = 2 - 10.5 \cos(\pi y)$  and the shock is initially located at  $x = 1$ . The boundary conditions are Poinot and Lele's non-reflecting outflow boundary conditions (Poinot and Lele 1992) in the  $x$ -direction and periodic in the  $y$ -direction. Viscous terms for the non-reflecting boundary conditions were neglected, as the  $x$ -component of the numerical viscosity is set to zero on the left and right boundaries to ensure proper exiting of the characteristics. The tangential component of the numerical viscosity was left unchanged, which is consistent with viscous extension of non-reflecting outflow boundary conditions (Poinot and Lele 1992).

In the case of two mixture components, the continuity equation is replaced by two mass conservation equations for each mixture

$$\frac{\partial \rho Y_i}{\partial t} + \frac{\partial \rho Y_i u_j}{\partial x_j} = 0, \quad (28)$$

where  $Y_i$  ( $i = 1, 2$ ) is the mass fraction of the two different mixture components, italic subscript  $j$  denotes different directions, and repeated indices imply the summation. After adding the diffusive terms Equation (28) becomes

$$\begin{aligned} \frac{\partial \rho Y_i}{\partial t} + \frac{\partial \rho Y_i u_j}{\partial x_j} \\ = \frac{1}{2} \sum_{k=1}^n \Delta x_k \frac{\partial}{\partial x_k} \left( \Phi C \frac{\partial \rho Y_i}{\partial x_k} \right). \end{aligned} \quad (29)$$

Recall that since there are two different values of  $\gamma$ , one for each component, the equation for the pressure (26) must be modified to use  $\gamma$  that is a function of the mass fractions  $Y_i$  and Atwood number

$$At = \frac{\rho_1 - \rho_2}{\rho_1 + \rho_2}. \quad (30)$$

Given that the interface is at thermal equilibrium we can define parameter  $\alpha$  based upon the density ratio as

$$\alpha = \frac{\rho_1}{\rho_2} = \frac{R_2}{R_1} = \frac{1 + At}{1 - At} \quad (31)$$



and the specific heat ratio of a two component gas as

$$\gamma = \frac{Y_1 C_{P1} + Y_2 C_{P2}}{Y_1 C_{V1} + Y_2 C_{V2}} \quad (32)$$

so that the mixture formulation for our two component gas  $\gamma$  is given by

$$\gamma = \frac{Y_1 \gamma_1 (\gamma_2 - 1) + Y_2 \gamma_2 (\gamma_1 - 1) \alpha}{Y_1 (\gamma_2 - 1) + Y_2 (\gamma_1 - 1) \alpha}. \quad (33)$$

Using this mixture formulation for the specific heat ratio  $\gamma$  the pressure Equation (26) remains unchanged.

The simulation was performed on a  $20 \times 10$  base grid with a maximum level of resolution  $j_{\max} = 7$  giving an effective grid of  $1280 \times 640$  points. Because of the fact that the initial shock is initiated as analytical discontinuity, some initial transient is observed at the shock's original location for the first few time steps. At a time of  $t = 0.75$  units, Figure 12 shows the density as the shock is refracted into the second medium. In the regions, where the shock interacts with the interface, it behaves much like the twin reflection–rarefaction observed in shock-bubble interaction problem (Karni 1996, Bagabir and Drikakis 2001). The figure shows the transmitted shock in gas 2, the side shock connecting the transmitted shock to the initial shock in gas 1, and the expansion fan trailing the interface. All shocks and contacts are well resolved and do not show any oscillations near them.

As time progresses, the refracted shock wave continues to move into gas 2 and reflects off the top and bottom boundaries. Figures 13 and 14 show the density and the viscosity coefficient  $|\Phi C|$  at a time of  $t = 1.25$  units. The artificial viscosity is localised around the shock and interface and that the instability

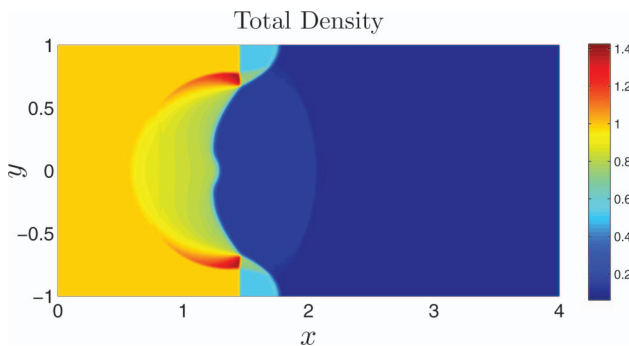


Figure 12. Interaction between the shock and the material interface. The plot shows the density at an output time of 0.75 units. There are no visible oscillations near the shock or contact and the interaction between the two is similar to the regular twin reflection–refraction seen in shock bubble interface problems.

is beginning to form at the centre of the material interface. Figure 15 shows the total density at a time of  $t = 2.65$  units. The typical mushroom-shape commonly associated with the Richtmyer–Meshkov instability forms with the vortices developing on the

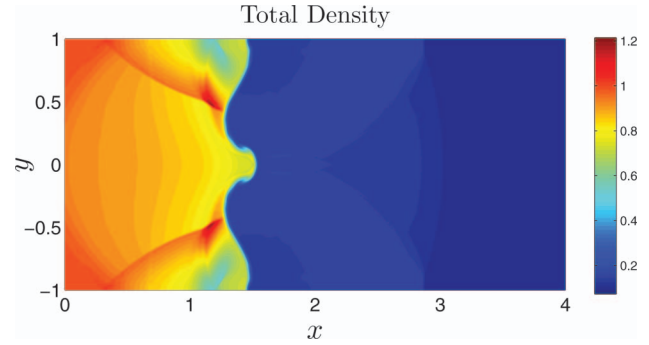


Figure 13. Density at an output time of 1.25 units. The shock has passed through into the other gas and has been refracted, which is why the reflections can be seen from the top and bottom boundaries. Notice the structure starting to form at the center of the interface.

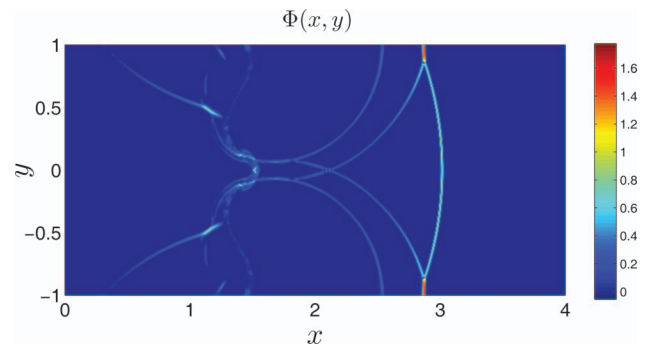


Figure 14. Plot of  $\Phi C$  at an output time of 1.25 units. The non-zero regions of  $\Phi C$  directly correlate with the discontinuity regions shown in Figure 13.

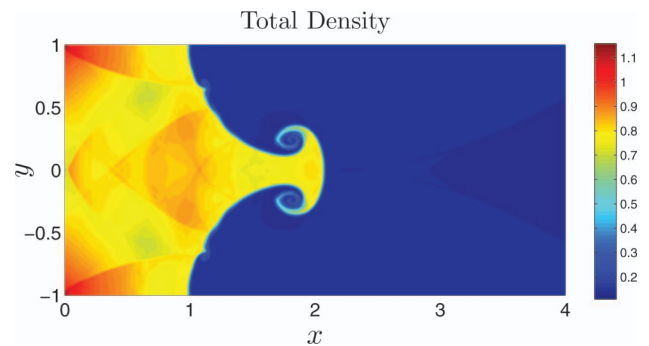


Figure 15. Density at an output time of 2.65 units. The shock has passed through the non-reflecting boundary but there is still some residual shock reflections in both gases although they are more visible in gas 1. The instability has taken its expected shape for Atwood number of 0.67.

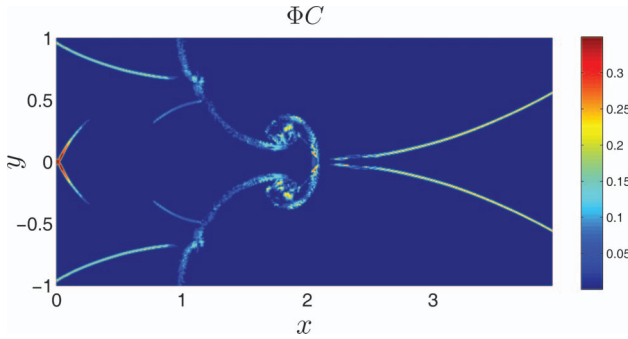


Figure 16. The  $\Phi C$  field at  $t = 2.65$  units. The intensity of the artificial viscosity in the vortex region becomes a non-negligible.

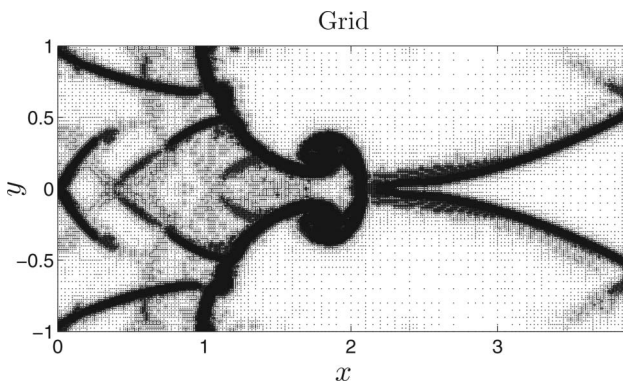


Figure 17. Computational grid at  $t = 2.65$  units. The points at the finest level of resolution are localised around the fine scale structures and where  $\Phi C$  is non-zero.

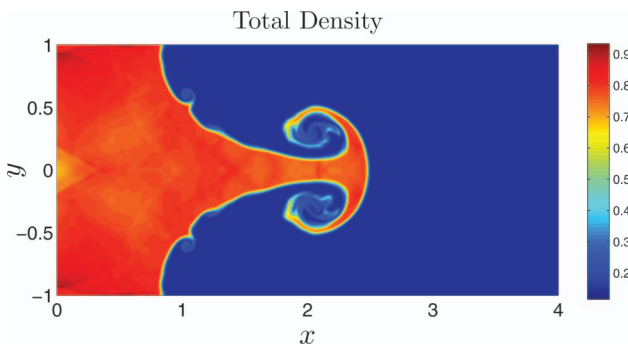


Figure 18. Smearing of small scale roll-up structures by numerical diffusion at much later time.

sides. Although the initial conditions are not exactly the same as (Abarzhi and Herrmann 2003), the shape of the instability is very similar. Figures 16 and 17 show the corresponding  $|\Phi C|$  and the grid at  $t = 2.65$  units. Notice that  $|\Phi C|$  becomes larger in the vortex region due to the fact that the finest level of resolution has been reached. Beyond this point, secondary instability results in creation of small scale

roll-up structures at the interface (e.g. Peng *et al.* 2003). If these structures are not fully resolved, they are smeared by numerical diffusion, as illustrated in Figure 18.

## 5. Conclusions

A simple numerical approach for solving hyperbolic conservation equations using the AWCN is presented, where a localised artificial viscosity is added in an explicit fashion in regions of discontinuity. The wavelet coefficients are used to create a shock/jump discontinuity locator function  $\Phi$ . Using this function, artificial viscosity is added explicitly using a conservative central differencing scheme. Numerical diffusion reduces the magnitudes of wavelet coefficients to a reasonable level after the discontinuity has passed. Once the wavelet coefficients at the finest level of resolution have been reduced below the prescribed error threshold value  $\epsilon$ , the artificial viscosity is shut off and any remaining physical waves are free to propagate undamped. Numerous test cases are presented and analysed to show efficiency, robustness and ease of extending the method to more complex problems. It is also shown that the artificial viscosity can be used as a general non-linear stabilisation technique for any AWCN simulation. Although the method uses more points across discontinuities than other high order methods such as HLLC, ENO, WENO, MUSCL, its use in conjunction with an adaptive grid makes it computationally efficient.

## Acknowledgements

Support for this work was provided by the National Science Foundation (NSF) under grants No. ACI-0242457 and CBET-0756046. This support is gratefully acknowledged.

## References

- Abarzhi, S.I. and Herrmann, M., 2003. New type of the interface evolution in the Richtmyer-Meshkov instability. *Center for Turbulence Research Annual Research Briefs*, 173–183.
- Alam, J., Kevlahan, N.R., and Vasilyev, O.V., 2006. Simultaneous space-time adaptive wavelet solution of nonlinear partial differential equations. *Journal of Computational Physics*, 214 (2), 829–857.
- Anuchina, N.N., *et al.*, 2004. Numerical simulations of Rayleigh-Taylor and Richtmyer-Meshkov instability using MAH-3 code. *Journal of Computational and Applied Mathematics*, 168, 11–20.
- Babuska, I., Chandra, J., and Flaherty, J.E., 1984. *Adaptive Computational methods for Partial differential equations*. Philadelphia: SIAM.
- Bagabir, A. and Drikakis, D., 2001. Mach number effects on shock-bubble interaction. *Shock Waves*, 11, 209–218.
- Bell, J., *et al.*, 1994. 3-Dimensional adaptive mesh refinement for hyperbolic conservation-laws. *SIAM Journal of Scientific Computing*, 15 (1), 127–138.

- Berger, M.J. and Colella, P., 1989. Local adaptive mesh refinement for shock hydrodynamics. *Journal of Computational Physics*, 82 (1), 64–84.
- Berger, M.J. and Leveque, R.J., 1998. Adaptive mesh refinement using wave-propagation algorithms for hyperbolic systems. *SIAM Journal of Numerical Analysis*, 35 (6), 2298–2316.
- Berger, M.J. and Oliger, J., 1984. Adaptive mesh refinement for hyperbolic partial-differential equations. *Journal of Computational Physics*, 53 (3), 484–512.
- Burger, R. and Kodakevicius, A., 2007. Adaptive multiresolution WENO schemes for multispecies kinematic flow models. *Journal of Computational Physics*, 224, 1190–1222.
- Chiavassa, G., Donat, R., and Müller, S., 2003. Multi-resolution-based adaptive schemes for hyperbolic conservation laws. In: T. Plewa, T. Linde, and V. Weiss, eds. *Adaptive mesh refinement theory and applications*, Vol. 41: *Lecture notes in computational science and engineering*. Berlin: Springer-Verlag, 137–159.
- Chui, C.K., 1997. *Wavelets: a mathematical tool for signal analysis*. SIAM Monographs on Mathematical Modeling and Computation. Philadelphia: SIAM.
- Cohen, A.M., et al., 2001. Fully adaptive multiresolution finite volume schemes for conservation laws. *Mathematics of Computation*, 72, 183–225.
- Colella, P., 1985. A direct Eulerian MUSCL scheme for gas-dynamics. *SIAM Journal on Scientific and Statistical Computing*, 6 (1), 104–117.
- Daubechies, I., 1992. *Ten lectures on wavelets*. No. 61 CBMS-NSF Series in Applied Mathematics Philadelphia: SIAM.
- Donoho, D.L., 1992. Interpolating wavelet transforms. Department of Statistics, Stanford University, Technical report 408.
- Flaherty, J.E., 1989. *Adaptive methods for partial differential equations*. Philadelphia: SIAM.
- Harten, A., 1983. High-resolution schemes for hyperbolic conservation-laws. *Journal of Computational Physics*, 49, 357–393.
- Harten, A., 1994. Adaptive multiresolution schemes for shock computations. *Journal of Computational Physics*, 115, 319–338.
- Harten, A., et al., 1997. Uniformly high order accurate essentially non-oscillatory schemes, 3. (Reprinted from *Journal of Computational Physics*, vol. 71, pg 231, 1987). *Journal of Computational Physics*, 131 (1), 3–47.
- Harten, A., Lax, P., and van Leer, B., 1983. On upstream differencing and Godunov-Type schemes for hyperbolic conservation law. *SIAM Review*, 25, 35–61.
- Karni, S., 1996. Hybrid multifluid algorithms. *SIAM Journal of Scientific Computation*, 17, 1019–1039.
- Kevlahan, N.K.R., Alam, J.M., and Vasilyev, O.V., 2007. Scaling of space-time modes with Reynolds number in two-dimensional turbulence. *Journal of Fluid Mechanics*, 570, 217–226.
- Kevlahan, N.K.R. and Vasilyev, O.V., 2005. An adaptive wavelet collocation method for fluidstructure interaction at high Reynolds numbers. *SIAM Journal of Scientific Computation*, 26 (6), 1894–1915.
- Laney, C.B., 1998. *Computational Gasdynamics*. New York: Cambridge University Press.
- Liou, M.S., 1996. A sequel to AUSM: AUSM(+). *Journal of Computational Physics*, 129 (2), 364–382.
- Liou, M.S. and Steffen, C.J., 1993. A New Flux Splitting Scheme. *Journal of Computational Physics*, 107 (1), 23–39.
- Liu, X.D., Osher, S., and Chan, T., 1994. Weighted essentially nonoscillatory schemes. *Journal of Computational Physics*, 115 (1), 200–212.
- Mallat, S., 1998. *A wavelet tour of signal processing*. Cambridge: Academic Press.
- Nithiarasu, P., et al., 1998. Shock capturing viscosities for the general fluid mechanics algorithm. *International Journal for Numerical Methods in Fluids*, 28, 1325–1353.
- Peng, G., Zabusky, N., and Zhang, S., 2003. Vortex-accelerated secondary baroclinic vorticity deposition and late-intermediate time dynamics of a two-dimensional Richtmyer-Meshkov interface. *Physics of Fluids*, 15 (12), 3730–3744.
- Poinsot, T. and Lele, S., 1992. Boundary conditions for direct simulations of compressible viscous flows. *Journal of Computational Physics*, 101, 104–129.
- Sjogreen, B. and Yee, H.C., 2000. *Multiresolution wavelet based adaptive numerical dissipation control for shock-turbulence computation*. Moffett Field, CA: NASA Ames Research Center. RIACS Technical Report TR01.01.
- Sweby, P.K., 1984. High resolution schemes using flux limiters for hyperbolic conservation laws. *SIAM Journal on Numerical Analysis*, 21, 995–1011.
- Sweldens, W., 1996. The lifting scheme: A custom-design construction of biorthogonal wavelets. *Applied and Computational Harmonic Analysis*, 3 (2), 186–200.
- Sweldens, W., 1998. The lifting scheme: a construction of second generation wavelets. *SIAM Journal of Mathematical Analysis*, 29 (2), 511–546.
- Toro, D.F., 1997. *Riemann solvers and numerical methods for fluid dynamics*. New York: Springer-Verlag.
- Van Leer, B., 1974. Towards the ultimate conservative difference scheme. II Monotonicity and conservation combined in a second-order scheme. *Journal of Computational Physics*, 14, 361–370.
- van Leer, B., 1979. Towards the ultimate conservative difference scheme, V. A second order sequel to Godunov's method. *Journal of Computational Physics*, 32 (1), 101–136.
- Vasilyev, O.V., 2003. Solving multi-dimensional evolution problems with localized structures using second generation wavelets. *International Journal of Computational Fluid Dynamics*, Special issue on *High-resolution methods in Computational Fluid Dynamics*, 17 (2), 151–168.
- Vasilyev, O.V. and Bowman, C., 2000. Second generation wavelet collocation method for the solution of partial differential equations. *Journal of Computational Physics*, 165, 660–693.
- Vasilyev, O.V. and Kevlahan, N.K.R., 2002. Hybrid wavelet collocation – Brinkman penalization method for complex geometry flows. *International Journal of Numerical Methods in Fluids*, 40, 531–538.
- Vasilyev, O.V. and Kevlahan, N.K.R., 2005. An adaptive multilevel wavelet collocation method for elliptic problems. *Journal of Computational Physics*, 206 (2), 412–431.
- Vasilyev, O.V. and Paolucci, S., 1996. A dynamically adaptive multilevel wavelet collocation method for solving partial differential equations in a finite domain. *Journal of Computational Physics*, 125, 498–512.
- Vasilyev, O.V. and Paolucci, S., 1997. A fast adaptive wavelet collocation algorithm for multi-dimensional PDEs. *Journal of Computational Physics*, 125, 16–56.

- Vasilyev, O.V., Paolucci, S., and Sen, M., 1995. A multilevel wavelet collocation method for solving partial differential equations in a finite domain. *Journal of Computational Physics*, 120, 33–47.
- Warren, G.P., *et al.*, 1991. Grid Convergence for adaptive methods. In: *AIAA 10th Computational Fluid Dynamics Conference*, 24–27 June 1991, Honolulu, HI AIAA – 1991–1592, 729–741.
- Warren, G.P., *et al.*, 1993. Grid convergence for adaptive methods. In: M. Baines and K.W. Morton, eds. *Numerical methods for fluid dynamics 4*. International Conference on Numerical Methods for Fluid Dynamics, Reading, England. Oxford: Clarendon Press, 317–328.
- Woodward, P. and Colella, P., 1984. The numerical simulation of two-dimensional fluid flow with strong shocks. *Journal Computational Physics*, 54, 115–173.
- Yamaleev, N. and Carpenter, M., 2002. On accuracy of adaptive grid methods for captured shocks. *Journal of Computational Physics*, 181 (1), 280–316.
- Yee, H.C., 1987. Construction of explicit and implicit symmetrical TVD schemes and their applications. *Journal of Computatonal Physics*, 68, 151–179.